A Comprehensive Spatial-Temporal Channel Propagation Model for the Ultra-Wideband Spectrum 2–8 GHz

Camillo Gentile, Sofia Martinez Lopez, and Alfred Kik
National Institute of Standards and Technology
Wireless Communication Technologies Group
Gaithersburg, Maryland, USA

Abstract— **Despite the potential for high-speed communications, stringent regulatory mandates on Ultra-Wideband (UWB) emission have limited its commercial success. By combining resolvable UWB multipath from different directions, Multiple-Input Multiple-Output (MIMO) systems can drastically improve link robustness or range. In fact, a plethora of algorithms and coding schemes already exist for UWB-MIMO systems, however these papers use simplistic channel models in simulation and testing. While the temporal characteristics of the UWB channel have been well documented, surprisingly there currently exists but a handful of spatial-temporal models to our knowledge, and only two for bandwidths in excess of 500 MHz. This paper proposes a comprehensive spatial-temporal model for the frequency spectrum 2–8 GHz, featuring many novel parameters. In order to extract the parameters, we conduct an extensive measurement campaign using a vector network analyzer coupled to a virtual circular antenna array. The campaign includes 160 experiments up to a non line-of-sight range of 35 meters in four buildings with construction material varying from sheetrock to steel.**

I. Introduction

Ultra-Wideband (UWB) technology is characterized by a bandwidth greater than 500 MHz or exceeding 20% of the center frequency of radiation [1]. Despite the potential for high-speed communications, the FCC mask of -41.3 dBm/MHz EIRP in the spectrum 3.1–10.6 GHz translates to a maximum transmission power of -2.6 dBm, limiting applications to moderate data rates or short range. Multiple-Input Multiple-Output (MIMO) communication systems exploit spatial diversity by combining multipath arrivals from different directions to drastically improve link robustness or range [2]. Ultra-Wideband lends to MIMO by enabling multipath resolution at the receiver through its fine time pulses; moreover, most UWB applications are geared towards indoor environments rich in scattering which provide an ideal reception scenario for MIMO implementation; in addition, the GHz center frequency relaxes the mutual-coupling requirements on the spacing between antenna array elements. For these reasons UWB and MIMO fit hand-in-hand, making the best possible use of radiated power to ensure the the commercial success of Ultra-Wideband communication systems.

In fact, a plethora of algorithms and coding schemes already exist for UWB-MIMO systems, exploiting not only spatial diversity, but time and frequency diversity as well [3], [4], [5]. Yet these papers use simplistic channel models in simulation and testing. While the temporal characteristics of the UWB channel have been well documented in [1], [6], [7], [8], [9], [10], [11], [12], [13], [14], surprisingly there currently exists but a handful of spatial-temporal channel models to our knowledge [15], [16], [17], [18], and only two for UWB with bandwidths in excess of 500 MHz [19], [20]. Most concentrate on separately characterizing a few parameters of the channel, but none furnish a comprehensive model in multiple environments which allows total reconstruction of the spatial-temporal response, analogous to the pioneering work in the UWB temporal model of Molisch et al. [1]. Specifically, the main contributions of this paper are:

- *a frequency-dependent pathloss model*: allows reconstructing the channel for any subband within f = 2–8 GHz, essential to test schemes using frequency diversity, and incorporates frequency-distance dependence previously modeled separately;
- *a spatial-temporal response model*: introduces the distinction between spatial clusters and temporal clusters, and incorporates spatial-temporal dependence previously modeled separately;
- *diverse construction materials*: to model typical building construction materials varying as sheet rock, plaster, cinder block, and steel rather than with building layout (i.e. office, residential typically have the same wall materials);
- *high dynamic range*: the high dynamic range of our system allows up to 35 meters in non line-of-sight (NLOS) range to capture the effect of interaction with up to 10 walls in the direct path between the transmitter and receiver.

The paper reads as follows: Section II describes the frequency and spatial diversity techniques we use to measure the spatial-temporal propagation channel. The subsequent section details the specifications of our measurement system realized through a vector network analyzer coupled to a virtual circular antenna array, and outlines our suite of measurements. The main section IV describes our proposed stochastic model to characterize the channel with parameters reported separately for eight different environments. Given the wealth of accumulated data furnished through our measurement campaign, we attempt to reconcile the sometimes contradictory findings amongst other models due to limited measurements, followed by conclusions in the last section.

II. Measuring the spatial-temporal response

A. Measuring the temporal response through frequency diversity

The temporal response $h(t)$ of the indoor propagation channel is composed from an infinite number of multipath arrivals indexed through k

$$h(t) = \left(\frac{d}{d_0}\right)^{-\frac{n}{2}} \left(\frac{f}{f_0}\right)^{-\frac{\alpha}{2}} \underbrace{\sum_{k=1}^{\infty} a_k e^{j\varphi_k} \delta(t-\tau_k)}_{\tilde{h}(t)}, \tag{1}$$

This full text paper was peer reviewed at the direction of IEEE Communications Society subject matter experts for publication in the IEEE "GLOBECOM" 2009 proceedings.

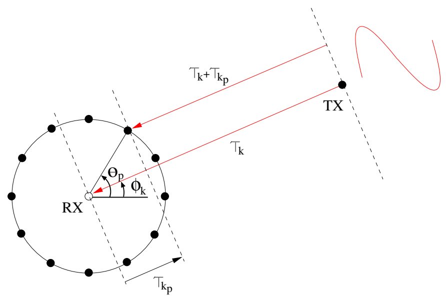

Fig. 1. The uniform circular array antenna.

where τ_k denotes the delay of the arrival in propagating the distance d between the transmitter and receiver, and the complex-amplitude $a_k e^{j\varphi_k}$ accounts for both attenuation and phase change due to reflection, diffraction, and other specular effects introduced by walls (and other objects) on its path. The attenuation coefficient n and the frequency parameter α represent the distance and frequency dependences of the *reference* temporal response $\tilde{h}(t)$ defined at reference point (d_0, f_0). Incorporating the frequency parameter has been shown to improve channel reconstruction up to 40% for bandwidths in excess of 2 GHz [21] relative to the conventional one which assumes $\alpha = 0$ [22].

The temporal response $h(t)$ has a frequency response

$$H(f) = \left(\frac{d}{d_0}\right)^{-\frac{n}{2}} \left(\frac{f}{f_0}\right)^{-\frac{\alpha}{2}} \sum_{k=1}^{\infty} a_k e^{j\varphi_k} e^{-j2\pi f \tau_k}, \qquad (2)$$

suggesting that the channel can be characterized through *frequency diversity*: we sample $H(f) = \frac{Y(f)}{X(f)}$ at rate Δf by transmitting tones $X(f)$ across the channel and then measuring $Y(f)$ at the receiver. Characterizing the channel in the frequency domain offers two important advantages over transmitting a UWB pulse and recording the temporal response directly: 1) it enables extracting the frequency parameter α; 2) a subband with bandwidth B and center frequency f_c can selected a posteriori in reconstructing the channel. The discrete frequency spectrum $X(f)$ transforms to a signal with period $\frac{1}{\Delta f}$ in the time domain [23]. Choosing Δf = 1.25 MHz allows for a maximum multipath spread of 800 ns, which proves sufficient throughout all four buildings for the arrivals to subside within one period and avoid time aliasing.

B. Measuring the spatial response through spatial diversity

Replacing the single antenna at the receiver with an antenna array introduces *spatial diversity* into the system. This enables measuring both the temporal and spatial properties of the UWB channel. For this purpose, we chose to implement the uniform circular array (UCA) over the uniform linear array (ULA) in light of the following two important advantages: 1) the azimuth of the UCA covers 360° in contrast to the 180° of the ULA; 2) the beam pattern of the UCA is uniform around the azimuth angle while that of the ULA broadens as the beam is steered from the boresight.

Consider the diagram in Fig. 1 of the uniform circular array. The P elements of the UCA are arranged uniformly around its perimeter of radius r, each at angle $\theta_p = \frac{2\pi i}{P}$, $p = 1 \ldots P$. The radius determines the half-power antenna aperture corresponding to $29.2° \frac{c}{r \cdot f}$ [24]. Let $H(f)$ be the frequency response of the channel between the transmitter and reference center of the receiver array. Arrival k approaching from angle ϕ_k hits element p with a delay $\tau_{k_p} = -\frac{r}{c}\cos(\phi_k + \theta_p)$ with respect to the center [25], hence the element frequency response $H_p(f)$ is a phase-shifted version of $H(f)$ by the steering vector, or

$$H_p(f) = H(f) e^{-j2\pi f \tau_{k_p}} = H(f) e^{j2\pi f \frac{r}{c}\cos(\phi_k + \theta_p)}. \qquad (3)$$

The array frequency response $H(f, \theta)$ is generated through beamforming by shifting the phase of each element frequency response $H_p(f)$ back into alignment at the reference [25]:

$$H(f, \theta) = \frac{1}{P} \sum_{p=1}^{P} H_p(f) e^{-j2\pi f \frac{r}{c}\cos(\theta + \theta_p)} \qquad (4)$$

The spatial-temporal response $h(t, \theta)$ can then be recovered through the Inverse Discrete Fourier Transform of its array frequency response as

$$h(t, \theta) = \frac{1}{\frac{B}{\Delta f}} \sum_{l=1}^{\frac{B}{\Delta f}} H(f, \theta) e^{j2\pi f t}, \qquad (5)$$

where $f = f_c - \frac{B}{2} + l \cdot \Delta f$.

The frequency-dependent pathloss is defined as

$$PL(f) = |H(f)|^2 = \frac{1}{P} \sum_{p=1}^{P} |H_p(f)|^2. \qquad (6)$$

III. The Channel Measurements

Fig. 2 displays the block diagram of our measurement system. The transmitter antenna is mounted on a tripod while the UCA was realized virtually by mounting the receiver antenna on a positioning table. We sweep the P = 97 elements of the array by automatically re-positioning the receiver at successive angles θ_p around its perimeter. At each element p, a vector network analyzer (VNA) in turn sweeps the discrete frequencies in the 2–8 GHz band. A total channel measurement, comprising the element sweep and the frequency sweep at each element, takes about 24 minutes. To eliminate disturbance due to the activity of personnel throughout the buildings and guarantee a static channel during the complete sweep, the measurements were conducted after working hours.

During the frequency sweep, the VNA emits a series of tones with frequency f at Port 1 and measures the relative amplitude and phase $S^{21}(f)$ with respect to Port 2, providing automatic phase synchronization between the two ports. The long cable enables variable placement of the transmitter and receiver antennas from each other throughout the test area. Their height was set to 1.7 m (average human height). The preamplifier and power amplifier on the transmit branch boost the signal such that it radiates at approximately 30 dBm from the antenna. After it passes through the channel, the low-noise amplifier (LNA) on the receiver branch boosts the signal above the noise floor of Port 2 before feeding it back. The dynamic range of the system corresponds to 140 dB as computed in [26] for an IF bandwidth of 1 kHz and a SNR of 15 dB at the receiver.

This full text paper was peer reviewed at the direction of IEEE Communications Society subject matter experts for publication in the IEEE "GLOBECOM" 2009 proceedings.

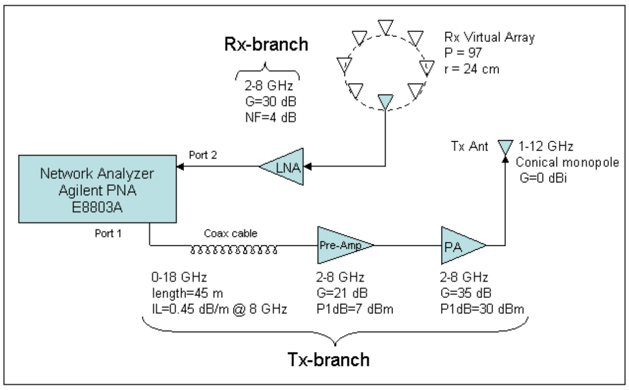

Fig. 2. The block diagram of the measurement system.

TABLE I
EXPERIMENTS CONDUCTED IN MEASUREMENT CAMPAIGN.

building	wall material	LOS range (10)	NLOS range (30)
NIST North	sheet rock / aluminum studs	4.2-23.4 m	7.2-35.1 m max wall#: 9
Child Care	plaster / wooden studs	2.6-15.3 m	7.8-32.4 m max wall#: 8
Sound	cinder block	7.4-43.7 m	2.4-32.5 m max wall#: 10
Plant	steel	7.2-41.7 m	2.1-34.2 m max wall#: 10

The $S_p^{21}(f)$-parameter of the network in Fig. 2 can be expressed as a product of the Tx-branch, the Tx-antenna, the propagation channel, the Rx-antenna, and the Rx-branch

$$\begin{aligned} S_p^{21}(f) &= H_{Tx}^{bra}(f) \cdot H_{Tx}^{ant}(f) \cdot H_p(f) \cdot H_{Rx}^{ant}(f) \cdot H_{Rx}^{bra}(f) \\ &= H_{Tx}^{bra}(f) \cdot \underbrace{H_{Tx}^{ant}(f) \cdot H_{Rx}^{ant}(f)}_{H^{ant}(f)} \cdot H_p(f) \cdot H_{Rx}^{bra}(f). \end{aligned} \tag{7}$$

The element frequency response H_p is extracted by individually measuring the transmission responses $H_{Tx}^{bra}, H_{Rx}^{bra}$, and H^{ant} in advance and deembedding them from (7).

The measurement campaign was conducted in four separate buildings on the NIST campus in Gaitherburg, Maryland, each constructed from a dominant wall material varying from sheet rock to steel. Table I summarizes the 40 experiments in each building (10 LOS and 30 NLOS), including the maximum number of walls separating the transmitter and receiver. The ground-truth distance d and ground-truth angle ϕ_0 between the transmitter and receiver were calculated in each experiment by pinpointing their coordinates on site with a laser tape, and subsequently finding these values using a computer-aided design (CAD) model of each building floor plan.

IV. THE PROPOSED SPATIAL-TEMPORAL MODEL

The proposed model for the spatial-temporal response $h(t, \theta)$ follows directly from (1) by augmenting the temporal response $h(t)$ in the θ dimension as

$$h(t,\theta) = \left(\frac{d}{d_0}\right)^{-\frac{n}{2}} \left(\frac{f}{f_0}\right)^{-\frac{\alpha}{2}} \tilde{h}(t,\theta), \tag{8}$$

the product of the path loss factor and the reference spatial-temporal response. This section describes the parameters of the two separately and outlines the pseudocode to reconstruct a stochastic channel response accordingly.

A. The frequency-dependent pathloss model

The pathloss model written explicitly as a function of d to account for the distance of each experiment follows by expanding (6) as

$$\begin{aligned} (a) \quad PL(d,f) &= \underbrace{PL(d_0,f_0)\left(\frac{d}{d_0}\right)^{-n}}_{PL(d,f_0)} \left(\frac{f}{f_0}\right)^{-\alpha}; \\ (b)\ PL(d_0,f_0) &= \sum_{k=1}^{\infty} a_k^2. \end{aligned} \tag{9}$$

The reference pathloss $PL(d_0, f_0)$ at d_0 = 1 m and the attenuation coefficient n were extracted at the center frequency f_0 = 5 GHz by fitting the model above to the data points of the experiments with varying distance given from (6). We found the breakpoint model below [9] to represent the data much more accurately.

$$PL(d,f_0) = \begin{cases} PL(d_0,f_0)\left(\frac{d}{d_0}\right)^{-n_0}, & d \le d_1 \\ PL(d_1,f_0)\left(\frac{d}{d_1}\right)^{-n_1}, & d > d_1 \end{cases} \tag{10}$$

Then frequency parameter α in (9a) was fit to the remaining data points by allowing the frequency to vary. Based on the Geometric Theory of Diffraction, in previous work [27] we observed that wall interactions such as transmission, reflection, and diffraction increase α from the free space propagation value of zero. The number of expected interactions increases with distance, justifying the linear dependence of the frequency parameter on d modeled as

$$\alpha(d) = \alpha_0 + \alpha_1 \cdot d, \tag{11}$$

with positive slope α_1 through all environments[1]. Fig. 4a illustrates the frequency parameter versus the distance for the experiments in the *Child Care* in NLOS environment.

B. The reference spatial-temporal response

Our model for the reference spatial-temporal response $\tilde{h}(t, \theta)$ essentially follows from (1) by augmenting $\tilde{h}(t)$ in the θ dimension as

$$\tilde{h}(t,\theta) = \sum_{i=1}^{N}\sum_{j=1}^{\infty}\sum_{k=1}^{\infty} a_{ijk} e^{j\varphi_{ijk}} \delta(t-\tau_{ijk}, \theta-\phi_{ijk}). \tag{12}$$

The measured responses $\tilde{h}(t, \theta)$ can be recovered by replacing $H(f, \theta)$ in (5) instead with $\tilde{H}(f,\theta) = H(f,\theta) \Big/ \left(\frac{d}{d_0}\right)^{-\frac{n}{2}} \left(\frac{f}{f_0}\right)^{-\frac{\alpha}{2}}$ which is

[1]Only *Child Care* in LOS exhibited a small negative slope due to lack of data where the building structure limited the longest LOS distance to only 15.3 m.

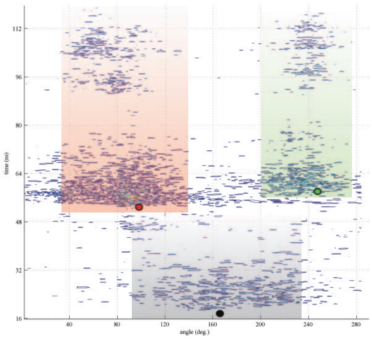

(a) The response

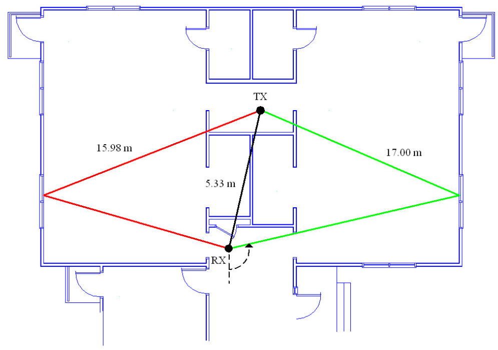

(b) The partial floor plan

Fig. 3. A measured spatial-temporal response in *Child Care* with three distinct superclusters.

normalized by the pathloss factor. Note that the parameters of the pathloss model in IV-A are necessary in order to generate $\tilde{h}(t,\theta)$ and so must be extracted a priori. Once generated, the arrival data points $(a_{ijk}, \varphi_{ijk}, \tau_{ijk}, \phi_{ijk})$ are extracted from the responses using the CLEAN algorithm in [16]. An average power threshold of 27 dB from the maximum peak in the response was used to isolate the most significant arrivals in fitting the model parameters in the sequel.

The reference spatial-temporal response in (12) partitions the arrivals indexed through k into N spatial clusters, or *superclusters* indexed through i, and temporal clusters, or simply *clusters* indexed through j. It reflects our measured responses composed consistently from 1) one *direct* supercluster arriving first from the direction of the transmitter; and 2) one or more *guided* superclusters arriving later from the door(s) when placing the receiver in a room or from the hallway(s) when placing it in a hallway; the rooms and hallways effectively guide the arrivals through, creating "corridors" in the response. Consider as an example the measured response in Fig. 3a taken in *Child Care* with three distinct superclusters highlighted in different colors. The partial floor plan in Fig. 3b shows the three corresponding paths colored accordingly and the coordinate (ϕ_i, τ_i) of each path appears as a dot on the response. The direct supercluster arrives first along the direct path and the later two along the guided paths from the opposite directions of the hallway. We model N for NLOS through the Poisson distribution[2] as

$$N \sim \mathcal{P}(\eta) \tag{13}$$

and set $N = 1$ for LOS[3]. The notion of clusters harks back to the well-known phenomenon witnessed in temporal channel modeling [1], [9], [29] caused by larger scatterers in the environment which induce a delay with respect to the first cluster within a supercluster. Notice the two distinct clusters of each guided supercluster in Fig. 3a.

1) The delay τ_{ijk}:

The equations in (14) govern the arrival delays. The delay τ_1 of the direct supercluster coincides with that of the first arrival. In LOS conditions, τ_1 equals the ground-truth delay $\tau_0 = \frac{d}{c}$, i.e. the time elapsed for the signal to travel the distance d at the speed of light c. However our previous work [30] confirms that the signal travels through walls at a speed slower than in free space, incurring an additional delay $(\tau_1 - \tau_0)$. As illustrated in Fig. 4b, the additional delay scales with τ_0 according to Ω in (14a) since the expected number of walls in the direct path increases with ground-truth delay. Based on the well-known Saleh-Valenzuela (S-V) model [29], the delay between guided superclusters $(\tau_i - \tau_{i-1}),\ i > 2$ depends on the randomly located doors or hallways and so obeys the exponential distribution[4] in (14a); so does the delay $(\tau_{ij} - \tau_{i,j-1})$ between clusters within supercluster i and the delay $(\tau_{ijk} - \tau_{ij,k-1})$ between arrivals within cluster ij due to randomly located larger and smaller scatterers respectively.

$$\begin{aligned}
&(a)\ (\tau_1 - \tau_0) = \Omega \cdot \tau_0,\ \ \tau_0 = \frac{d}{c};\\
&\quad\ (\tau_i - \tau_{i-1}) \sim \mathcal{E}(L),\ \ i > 2\\
&(b)\ (\tau_{ij} - \tau_{i,j-1}) \sim \mathcal{E}(\Lambda),\ \ \tau_{n0} = \tau_n\\
&(c)\ (\tau_{ijk} - \tau_{ij,k-1}) \sim \mathcal{E}(\lambda),\ \ \tau_{ij0} = \tau_{ij}
\end{aligned} \tag{14}$$

2) The angle ϕ_{ijk}:

As the walls retard the delay of the direct supercluster τ_1, they also deflect its angle ϕ_1 from the ground-truth angle ϕ_0 through refraction and diffraction. Our previous work [30] reveals that the degree of deflection also scales with τ_0 according to ω in (15a). Concerning the angle of the guided superclusters $\phi_i, i > 2$, our experiments confirm the uniform distribution in (15a) supported by the notion that the rooms and hallways could fall at any angle with respect to the orientation of the receiver. The cluster angle ϕ_{ij} approaches at the same angle as the supercluster due to the guiding effect of the rooms and hallways, and in agreement with [15], [16], [17] the Laplacian distribution[5] models the intra-cluster angle $(\phi_{ijk} - \phi_{ij})$, i.e. the deviation of the arrival angle from the cluster angle in (15c).

[2] $\mathcal{P}(\eta) = \frac{\eta^N e^{-\eta}}{N!}$

[3] We actually observed two superclusters in all our LOS experiments, however the second arriving with an offset of 180^o relative to the first was clearly due to the reflections off the opposite walls attributed to our testing configuration in the hallways rather than to the channel.

[4] $\mathcal{E}(L) = \frac{1}{L} e^{-\frac{(\tau_i - \tau_{i-1})}{L}}$

[5] $\mathcal{L}(\sigma) = \frac{1}{2\sigma} e^{-\frac{|\phi_{ijk} - \phi_{ij}|}{\sigma}}$

This full text paper was peer reviewed at the direction of IEEE Communications Society subject matter experts for publication in the IEEE "GLOBECOM" 2009 proceedings.

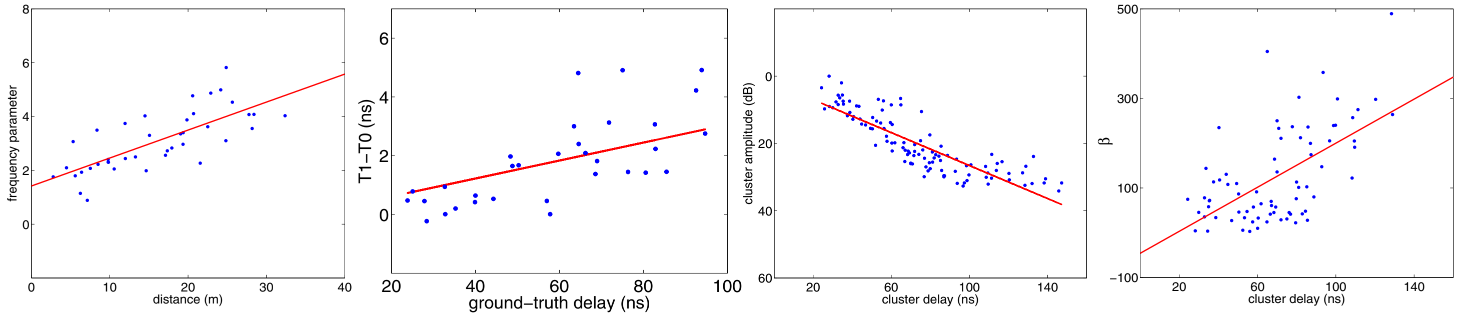

(a) frequency parameter vs. distance (b) $\tau_1 - \tau_0$ vs. cluster delay (c) cluster amplitude vs. cluster dela (d) β vs. cluster delay

Fig. 4. Illustration of selected model parameters for the *Child Care* in NLOS environment.

$$
\begin{aligned}
&(a)\ |\phi_1 - \phi_0| = \omega \cdot \tau_0; \\
&\quad \phi_i \sim \mathcal{U}[0, 2\pi),\ i > 2 \\
&(b)\ \phi_{ij} = \phi_i \\
&(c)\ (\phi_{ijk} - \phi_{ij}) \sim \mathcal{L}(\sigma)
\end{aligned} \tag{15}
$$

3) The complex amplitude $a_{ijk}e^{j\varphi_{ijk}}$:

The equations in (16) govern the arrival amplitudes. Like in the S-V model, the cluster amplitude a_{ij} fades exponentially versus the cluster delay τ_{ij} according to Γ, as illustrated in Fig. 4c; the arrival amplitude a_{ijk} also fades exponentially versus the intra-cluster delay $(\tau_{ijk} - \tau_{ij})$ according to $\gamma(\tau_{ij})$ in (16b). Our experiments suggest a linear dependence of γ on τ_{ij} in some buildings confirmed by other researchers [1], [9]. The parameter s drawn from a Normal distribution $\mathcal{N}(0, \sigma_s)$ quantifies the deviation between our model and the measured data and in that capacity represents the stochastic nature of the amplitude, of particular use when simulating time diversity systems [5]. The arrival phase φ_{ijk} is well-established in literature as uniformly distributed [23].

$$
\begin{aligned}
&(a)\ a_{ij} = a_{11} \cdot e^{-\frac{1}{2}\frac{(\tau_{ij} - \tau_{11})}{\Gamma}} \\
&(b)\ a_{ijk} = a_{ij} \cdot e^{-\frac{1}{2}\left[\frac{(\tau_{ijk} - \tau_{ij})}{\gamma(\tau_{ij})} + \frac{|\phi_{ijk} - \phi_{ij}|}{\beta(\tau_{ij})} + s\right]}; \\
&\quad \gamma(\tau_{ij}) = \gamma_0 + \gamma_1 \cdot \tau_{ij}, \\
&\quad \beta(\tau_{ij}) = \beta_0 + \beta_1 \cdot \tau_{ij}, \\
&\quad s \sim \mathcal{N}(0, \sigma_s) \\
&(c)\ \varphi_{ijk} \sim \mathcal{U}[0, 2\pi)
\end{aligned} \tag{16}
$$

We found the arrival amplitude a_{ijk} also to fade exponentially versus the the intra-cluster angle $|\phi_{ijk} - \phi_{ij}|$ according to $\beta(\tau_{ij})$ in (16b). In NLOS the walls spread the arrival amplitude in angle with each interaction on the path to the receiver. The number of expected interactions increases with the cluster delay, justifying a linear dependence of β on τ_{ij} as modeled through (16b). Fig. 4d illustrates this phenomenon for the *Child Care* in NLOS environment. However we exercise caution in generalizing this phenomenon as indeed it depends on the construction material: even though the sheetrock walls in *NIST North* promote the best signal penetration of the four buildings, the aluminum studs inside the walls spaced every 40 cm act as "spatial filters", reflecting back those arrivals most deviant from the cluster angle and hence sharpening the clusters in angle with increasing cluster delay, as indicated through negative β_1. This dependence is less noticeable in *Sound* and *Plant* where we record β_1 an order of magnitude less in comparison to the other two buildings because the signal propagates poorly through cinder block and steel respectively, and so wave guidance defaults as the chief propagation mechanism. In the past, Spencer [15], Cramer [16], and Chong [17] have claimed spatial-temporal independence; for Spencer, these conclusions were drawn from experiments conducted in buildings with concrete and steel walls similar to *Sound* and *Plant* respectively, where we too notice scarce dependence; for Chong and Cramer, the dependence was less observable because the experiments were conducted at a maximum distance of 14 m.

C. *Reconstructing the spatial-temporal response*

A spatial-temporal response can be reconstructed from our model through the following steps:

1) Select d and in turn $\tau_0 = \frac{d}{c}$, ϕ_0, and the parameters from one of the eight environments in Table II;
2) Generate the stochastic variables N and (a_{ijk}, φ_{ijk}, τ_{ijk}, ϕ_{ijk}) of the arrivals from Section IV-B; Set $a_{11} = 1$ in (16a) and then normalize the amplitudes to satisfy (9b); Keep only those clusters and arrivals with amplitude above a selected threshold;
3) Select a subband in f = 2–8 GHz with bandwidth B and center frequency f_c, and Δf; Compute $H(f)$ in (2) for each sample from the pathloss model in Section IV-A and the generated arrivals;
4) Select P and compute $H_p(f)$ in (3) from $H(f)$ for each element in the circular antenna array[6];
5) Compute $H(f,\theta)$ in (4) from $H_p(f)$ which yields the sought spatial-temporal response $h(t,\theta)$ through (5) by synthesizing all the frequencies in the subband.

V. Conclusions

We propose a detailed spatial-temporal channel model with 19 parameters for the UWB spectrum 2–8 GHz in eight different environments. The parameters were fit through an extensive measurement campaign including 160 experiments using a vector

[6]Note that any array shape can be used by applying the appropriate steering vector.

TABLE II

MODEL PARAMETERS FOR THE EIGHT ENVIRONMENTS.

environment		pathloss						N	delay				angle		amplitude					
	building	$PL(d_0,f_0)$ (dB)	n_0	n_1	d_1 (m)	α_0	α_1 (m^{-1})	η	Ω	L (ns)	Λ (ns)	λ (ns)	ω (^{o}/ns)	σ (^{o})	Γ (ns)	γ_0 (ns)	γ_1	β_0 (^{o})	β_1 (^{o}/ns)	σ_s (dB)
NLOS	*NIST North*	39.3	2.2	6.0	11	1.7	.015	2.0	0.01	6.2	25.2	0.82	0.13	32.1	22.6	47	.015	230	-1.4	2.8
NLOS	*Child Care*	45.4	2.0	6.3	10	1.4	.100	1.9	0.03	11.7	19.5	0.60	0.16	40.9	8.9	-9	.480	-46	2.5	2.9
NLOS	*Sound*	36.0	3.5	5.3	10	2.5	.031	2.0	0.06	9.5	15.5	0.86	0.31	29.1	11.7	6	.190	57	0.4	3.0
NLOS	*Plant*	47.5	1.4	NA	NA	1.9	.030	1.6	0.52	36.0	28.4	0.71	0.49	43.3	32.1	53	-.094	170	0.3	3.2
LOS	*NIST North*	43.7	1.0	NA	NA	0.7	.098	NA	0.00	NA	28.1	0.76	0.00	12.1	48.7	3.3	.000	18	0.0	5.4
LOS	*Child Care*	33.6	2.4	NA	NA	1.5	-.027	NA	0.00	NA	NA	0.14	0.00	6.9	20.8	0.5	.000	8	0.0	4.1
LOS	*Sound*	39.5	1.7	NA	NA	1.1	.053	NA	0.00	NA	NA	0.44	0.00	11.5	28.7	3.3	.000	25	0.0	4.2
LOS	*Plant*	47.5	1.4	NA	NA	1.6	.033	NA	0.00	NA	40.5	1.42	0.00	25.5	29.5	14.6	.000	153	0.0	3.9

network analyzer coupled to a virtual circular antenna array. The novelty of the model captures the dependence of the frequency parameter, the delay and angle of the first arrival, and the cluster shape on the signal propagation delay. Most importantly for UWB-MIMO systems, our model discriminates between clusters arriving from the direct path along the direction of the transmitter and those guided through doors and hallways.

REFERENCES

[1] A.F. Molisch, K. Balakrishnan, D. Cassioli, C.-C. Chong, S. Emami, A. Fort, J. Karedal, J. Kunisch, H. Schantz, U. Schuster, and K. Siwiak, "A Comprehensive Model for Ultrawideband Propagation Channels," *IEEE Global Communications Conf.*, pp. 3648-3653, March 2005.

[2] H.A. Khan, W.Q. Malik, D.J. Edwards, C.J. Stevens, "Ultra Wideband Multiple-Input Multiple-Output Radar," *IEEE Radar Conference*, pg. 900-904, May 2005.

[3] W.P. Siriwongpairat, W. Su, M. Olfat, and K.J.R. Liu, "Multiband-OFDM MIMO Coding Framework for UWB Communications Systems," *IEEE Trans. on Signal Processing*, vol. 54, no. 1, Jan. 2006.

[4] L. Yang and G.B. Giannakis, "Analog Space–Time Coding for Multi-antenna Ultra-Wideband Transmissions," *IEEE Trans. on Communications*, vol. 52, no. 3, March 2004.

[5] A. Sibille, "Time-Domain Diversity in Ultra-Wideband MIMO Communications," *EURASIP Journal on Applied Signal Processing*, vol. 3, pg. 316-327, 2005.

[6] Z. Irahhauten, H. Nikookar, and G.J.M. Janssen, "An Overview of Ultra Wide Band Indoor Channel Measurements and Modeling," *IEEE Microwave and Wireless Components Letters*, vol. 14, no. 8, Aug. 2004.

[7] S.S. Ghassemzadeh, L.J. Greenstein, T. Sveinsson, A. Kavcic, and V. Tarokh, "UWB Delay Profile Models for Residential and Commercial Indoor Environments," *IEEE Trans. on Vehicular Technology*, vol. 54, no. 4, July 2005.

[8] D. Cassioli, A. Durantini, and W. Ciccognani, "The Role of Path Loss on the Selection of the Operating Band of UWB Systems," *IEEE Conf. on Personal, Indoor and Mobile Communications*, pp. 3414-3418, June 2004.

[9] D. Cassioli, M.Z. Win, and A.F. Molisch, "The Ultra-Wide Bandwidth Indoor Channel: From Statistical Model to Simulations," *IEEE Journal on Selected Areas in Communications*, vol. 20, no. 6, Aug. 2002.

[10] S.M. Yano, "Investigating the Ultra-Wideband Indoor Wireless Channel," *IEEE Conf. on Vehicular Technology, Spring*, pp. 1200-1204, May 2002.

[11] C. Prettie, D. Cheung, L. Rusch, and M. Ho, "Spatial Correlation of UWB Signals in a Home Environment," *IEEE Conf. on Ultra Wideband Systems and Technologies*, pp. 65-69, May 2002.

[12] A. Durantini, W. Ciccognani, and D. Cassioli, "UWB Propagation Measurements by PN-Sequence Channel Sounding," *IEEE Conf. on Communications*, pp. 3414-3418, June 2004.

[13] A. Durantini and D. Cassioli, "A Multi-Wall Path Loss Model for Indoor UWB Propagation," *IEEE Conf. on Vehicular Technology, Spring*, pp. 30-34, May 2005.

[14] J. Kunisch and J. Pump, "Measurement Results and Modeling Aspects for the UWB Radio Channel," *IEEE Conf. on Ultra Wideband Systems and Technologies*, pp. 19-24, May 2002.

[15] Q.H. Spencer, B.D. Jeffs, M.A. Jensen, and A.L. Swindlehurst, "Modeling the Statistical Time and Angle of Arrival Characteristics of an Indoor Multipath Channel," *IEEE Journal on Selected Areas in Communications*, vol. 18, no. 3, March 2000.

[16] R.J.-M. Cramer, R.A. Scholtz, and M.Z. Win, "Evaluation of an Ultra-Wide-Band Propagation Channel," *IEEE Trans. on Antennas and Propagation*, vol. 50, no. 5, May 2002.

[17] C.-C. Chong, C.-M. Tan, D.I. Laurenson, S. McLaughlin, M.A. Beach, and A.R. Nix, "A New Statistical Wideband Spatio-Temporal Channel Model for 5-Ghz Band WLAN Systems," *IEEE Journal on Selected Areas in Communications*, vol. 21, no. 2, Feb. 2003.

[18] K. Haneda, J.-I. Takada, and T. Kobayashi, "Cluster Properties Investigated From a Series of Ultrawideband Double Directional Propagation Measurements in Home Environments," *IEEE Trans. on Antennas and Propagation*, vol. 54, no. 12, Dec. 2006.

[19] A.S.Y. Poon and M. Ho, "Indoor Multiple-Antenna Channel Characterization from 2 to 8 GHz," *IEEE Conf. on Communications*, May 2003.

[20] S. Venkatesh, V. Bharadwaj, and R.M. Buehrer, "A New Spatial Model for Impulse-Based Ultra-Wideband Channels," *IEEE Vehicular Technology Conference, Fall*, Sept. 2005.

[21] W. Zhang, T.D. Abhayapala, and J. Zhang, "UWB Spatial-Frequency Channel Characterization," *IEEE Vehicular Technology Conference, Spring*, May 2006.

[22] H. Hashemi, "The Indoor Radio Propagation Channel," *Proceedings of the IEEE*, vol. 81, no. 7, pp. 943-968.

[23] X. Li. and K. Pahlavan, "Super-Resolution TOA Estimation With Diversity for Indoor Geolocation," *IEEE Trans. on Wireless Communications*, vol. 3, no. 1, Jan. 2004.

[24] C.A. Balanis, "Antenna Theory: Analysis and Design, Second Edition" *John Wiley & Sons, Inc.*, 1997.

[25] T.B. Vu, "Side-Lobe Control in Circular Ring Array," *IEEE Trans. on Antennas and Propagation*, vo. 41, no. 8, Aug. 1993.

[26] J. Keignart and N. Daniele, "Subnanosecond UWB Channel Sounding in Frequency and Temporal Domain," *IEEE Conf. on Ultra Wideband Systems and Technologies*, pp. 25-30, May 2002.

[27] C. Gentile and A. Kik, "A Frequency-Dependence Model for the Ultra-Wideband Channel based on Propagation Events," *IEEE Global Communications Conf.*, Nov. 2007.

[28] C. Gentile and A. Kik, "A Comprehensive Evaluation of Indoor Ranging Using Ultra-Wideband Technology," *EURASIP Journal on Wireless Communications and Networking*, vol. 2007, id. 86031, 2007.

[29] A. Saleh and R.A. Valenzuela, "A statistical model for indoor mulipath propagation," *IEEE Journal on Selected Areas of Communications*, vol. 5, pp. 128-137, Feb. 1987.

[30] C. Gentile, A. Judson Braga, and A. Kik, "A Comprehensive Evaluation of Joint Range and Angle Estimation in Ultra-Wideband Location Systems for Indoors," *IEEE Conf. on Communications*, May 2008.

This full text paper was peer reviewed at the direction of IEEE Communications Society subject matter experts for publication in the IEEE "GLOBECOM" 2009 proceedings.